Cell Reports
Physical Science

CellPress
OPEN ACCESS

Article

Dynamic studies of antibody-antigen interactions with an electrolyte-gated organic transistor

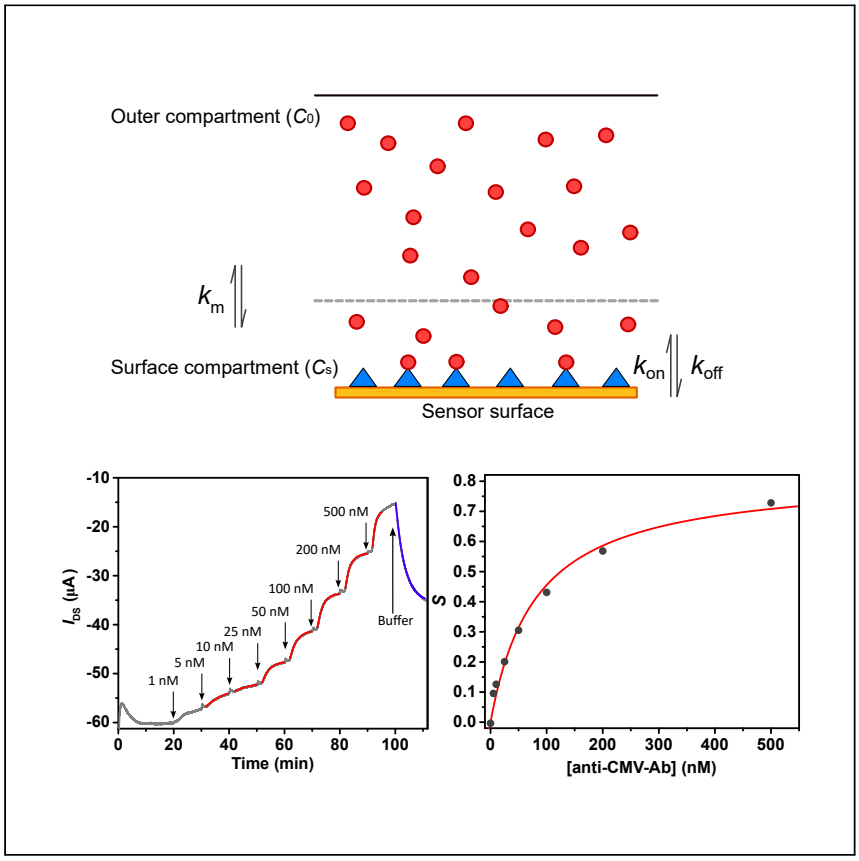

Electrolyte-gated organic transistors are ultrasensitive label-free biosensors. By exploiting this sensitivity, Manco Urbina et al. characterize the analyte binding kinetics on the sensor surface by real-time monitoring of the sensor response. The analysis of this response allowed them to detect small variations in the binding site affinities on the electrode surface.

Pamela Allison Manco Urbina, Alessandro Paradisi, Roger Hasler, ..., Wolfgang Knoll, Carlo Augusto Bortolotti, Fabio Biscarini

alessandro.paradisi@unimore.it (A.P.)
carloaugusto.bortolotti@unimore.it (C.A.B.)

Highlights

Study of analyte binding on electrode surface with electrolyte-gated transistors

The real-time sensing allows determination of the binding kinetics and thermodynamics

EGOTs' high sensitivity allows detection of small variations in binding constants

Manco Urbina et al., Cell Reports Physical Science 5, 101919
June 19, 2024 © 2024 The Authors. Published by Elsevier Inc.
https://doi.org/10.1016/j.xcrp.2024.101919

Please cite this article in press as: Manco Urbina et al., Dynamic studies of antibody-antigen interactions with an electrolyte-gated organic transistor, Cell Reports Physical Science (2024), https://doi.org/10.1016/j.xcrp.2024.101919

Cell Reports
Physical Science

CellPress
OPEN ACCESS

Article

Dynamic studies of antibody-antigen interactions with an electrolyte-gated organic transistor

Pamela Allison Manco Urbina,[1] Alessandro Paradisi,[1,*] Roger Hasler,[2,3] Matteo Sensi,[1] Marcello Berto,[1] Gulseren Deniz Saygin,[4] Jakub Dostalek,[2,3,5] Marcello Pinti,[1] Pierpaolo Greco,[4,6] Marco Borsari,[7] Wolfgang Knoll,[2,3] Carlo Augusto Bortolotti,[1,8,*] and Fabio Biscarini[1,4]

SUMMARY

Affinity-based biosensors employing surface-bound biomolecules for analyte detection are important tools in clinical diagnostics and drug development. In this context, electrolyte-gated organic transistors (EGOTs) are emerging as ultrasensitive label-free biosensors. In this study, we present an EGOT sensor integrated within a microfluidic system. The sensor utilizes the cytomegalovirus (CMV) phosphoprotein 65 as a biorecognition element to detect the pathological biomarker human anti-cytomegalovirus antibody in solution. The biorecognition element is grafted onto the gate electrode by exploiting the polyhistidine-tag technology. Real-time monitoring of the EGOT response, coupled with a two-compartment kinetic model analysis, enables the determination of analyte concentration, binding kinetics, and thermodynamics of the interaction. The analysis of the relevant kinetic parameters of the binding process yields a reliable value for the thermodynamic equilibrium constant and suggests that the measured deviations from the Langmuir binding model arise from the co-existence of binding sites with different affinities toward the antibodies.

INTRODUCTION

Affinity-based biosensors, exploiting surface-bound biomolecules as recognition elements for analytes in solution,[1] are becoming important and widely investigated for development of clinical diagnostics and for drug development studies.[2–4] In recent years, electrolyte-gated transistor (EGT) devices have emerged as promising candidates for biosensing applications.[4–6] They operate on channels with conjugated organic (semi)conductor thin films (in this case termed EGOTs),[7,8] carbon allotropes (e.g., carbon nanotubes, graphene),[9–14] or related forms, like reduced graphene oxide (rGO-EGT),[10,15–17] coupled by an electrolyte solution to the gate electrode. The most common device architecture for sensing exhibits the gate electrode functionalized with biorecognition moieties: an antibody, an aptamer, or an enzyme, depending on the nature of the target analyte.[4,18,19] EGTs are label-free sensors and hence do not require secondary reagents to detect binding of the analytes at the biorecognition interface. EGTs respond with the modulation of electronic current in reaction to ion-(semi)conductor interactions, controlled by the recognition-induced voltage change at the gate electrode.[4,8,20,21] The ion/(semi)conductor interactions occur both at the interface between the electrolyte and the (semi) conductor channel and inside the (semi)conductor channel, depending on the ion permeability of the (semi)conductor used as channel material.[8,20,22,23]

[1]Department of Life Sciences, Università di Modena e Reggio Emilia, Via Campi 103, 41125 Modena, Italy

[2]AIT Austrian Institute of Technology GmbH, Giefinggasse 4, 1210 Vienna, Austria

[3]Laboratory for Life Sciences and Technology (LiST), Faculty of Medicine and Dentistry, Danube Private University, Steiner Landstraße 124, 3500 Krems an der Donau, Austria

[4]Center for Translational Neurophysiology of Speech and Communication, Istituto Italiano di Tecnologia, Via Fossato di Mortara 17-19, 44121 Ferrara, Italy

[5]FZU-Institute of Physics, Czech Academy of Sciences, Na Slovance 1999/2, 182 21 Prague, Czech Republic

[6]Dipartimento di Neuroscienze e Riabilitazione, Università di Ferrara, Via Fossato di Mortara 19, 44121 Ferrara, Italy

[7]Department of Chemical and Geological Sciences, Università di Modena e Reggio Emilia, Via Campi 103, 41125 Modena, Italy

[8]Lead contact

*Correspondence:
alessandro.paradisi@unimore.it (A.P.),
carloaugusto.bortolotti@unimore.it (C.A.B.)

https://doi.org/10.1016/j.xcrp.2024.101919

This is an open access article under the CC BY-NC-ND license (http://creativecommons.org/licenses/by-nc-nd/4.0/).

Please cite this article in press as: Manco Urbina et al., Dynamic studies of antibody-antigen interactions with an electrolyte-gated organic transistor, Cell Reports Physical Science (2024), https://doi.org/10.1016/j.xcrp.2024.101919

Here we challenge EGTs with the clinical problem of rapid virus detection, specifically, human cytomegalovirus (CMV) antibodies, to demonstrate the first EGOT sensor for CMV infection. Human CMV is a prevalent betaherpesvirus infecting more than half of the western population and 80%–90% of those over 65 years[24] CMV infection has been shown to induce production of pro-inflammatory cytokines by leukocytes like interleukin 6 (IL-6) and tumor necrosis factor α (TNF-α).[25] Once infection is established, a strong specific immune response for CMV is elicited, which includes antibodies against structural tegument proteins, such as phosphoprotein 65. However, the immune system is not able to eradicate the virus, and the subject remains chronically infected. Even though CMV infection is typically unnoticed in healthy people, CMV seropositivity is associated with increased all-cause mortality in elderly people and can be life threatening for immunocompromised subjects, such as HIV-infected persons, organ transplant recipients, or newborn infants.[24,26,27]

Most of the sensing studies with EGTs rely on steady-state multiparametric characterization of the transfer curves as a function of the target analyte concentration. The dose curve can be constructed by correlating the change in one or more parameters with the concentration of the analyte.[28–31] For instance, the relative change in current at a fixed gate voltage (generally referred to as signal) vs. analyte concentration may be reconducted to binding isotherms to extract thermodynamic parameters (like free energy of binding). This approach implicitly assumes that the EGT sensor is at thermochemical equilibrium with the electrolyte solution and that the measured signal is linear with the population of the recognition sites; although reasonable, these two assumptions are not always obvious.

Recent research efforts were focused toward increasing the sensitivity and the limit of detection (LOD) reduction of these devices to allow detection of ultralow analyte concentrations. Recent reports demonstrated the possibility of detecting single molecules (zeptomolar [zM] concentration range) for millimeter-sized devices based on EGOT architecture.[30,32] To achieve such a high sensitivity, the channel or the gate electrode functionalization strategies need to yield a high density of surface-bound receptors ($\sim 10^{11}$–10^{12} sites cm^{-2}) for the target analyte. This implies that an efficient binding with small sample volumes and low analyte concentrations is accessible.[4,19,30] However, in the study of binding thermodynamics, the choice of the binding model used to interpret the experimental data is crucial and, often, due to the discretization of the sampling, ambiguous.[33] To correctly extract the thermodynamic parameters from the dose curve it is necessary to understand the dynamic behavior of the analyte-receptor interactions. This can be done by means of the time evolution of the current. This feature makes EGTs an attractive tool to study the binding kinetics of a biomolecular target (e.g., proteins, DNAs, and small molecules) to a specific binding site grafted at the functionalized electrode surface.[28,33–37] However, this analysis relies on a kinetic model of binding to interpret the data. In addition, since the time-dependent current is composed of many more points than those available in steady-state measurements, in principle, the relevant properties (including actual equilibrium constants) can be estimated with smaller errors.

In this work, we carry out both steady-state and kinetic measurements of an EGOT sensor designed to recognize anti-CMV antibodies (anti-CMV-Abs) with a PEDOT:PSS channel and a gate electrode functionalized with the CMV phosphoprotein 65 (CMV-pp65), which is a biological target of the human anti-CMV-Abs. We bind CMV-pp65 to the transistor gate electrode with an efficient functionalization strategy that exploits the polyhistidine-tag technology (which was originally developed for recombinant proteins) as a protein surface-immobilization method. Then, we integrate

Please cite this article in press as: Manco Urbina et al., Dynamic studies of antibody-antigen interactions with an electrolyte-gated organic transistor, Cell Reports Physical Science (2024), https://doi.org/10.1016/j.xcrp.2024.101919

CellPress
OPEN ACCESS

the EGOT biosensor into a microfluidics system, which allows a real-time recording of the biosensor's response to increasing concentrations of anti-CMV-Abs.

We analyze the time-dependent current in terms of the binding kinetics of the analyte on the gate electrode surface by means of the two-compartment model (TCM).[38] We demonstrate that the effective kinetic rate of the time varying EGOT current has, in general, a non-linear dependence on the analyte concentration due to the interdependence between elementary kinetic constants, density of binding sites, and mass transport at the interface. The observed trend can be simply interpreted in terms of two coexisting binding site populations, with different affinities toward the target. Our work demonstrates the extreme sensitivity of the time-dependent experiments to subtleties of the binding kinetics. These insights on the kinetics require modeling of the time-dependent experiments with EGOT sensors, provide quantitative assessment of the response time of the biosensor based on the recognition architecture, and potentially help us to identify routes to enhance sensitivity.

RESULTS AND DISCUSSION

Assessment of gate functionalization with surface plasmon resonance (SPR) and electrochemical techniques

The EGOT-based biosensor was constructed using a top-gate bottom-contact configuration, employing a gold gate electrode and operating in a microfluidic flow cell. To enable detection of anti-CMV-Abs in solution, we endowed the gate electrode with recognition capabilities by immobilizing the viral protein CMV-pp65. To do this, we exploited the well-established principle of metal-ion-affinity chromatography, commonly employed to purify recombinant proteins. Briefly, this technique involves the selective binding of a strand of six histidine residues (typically located at either the C or the N terminus of the amino acid chain) to a divalent cation (such as Ni^{2+} or Cu^{2+}) chelated to the solid phase of a chromatographic resin. Here, we employed this strategy to functionalize the gate electrode surface with the recombinant protein CMV-pp65, by adapting a methodology reported by Knoll and co-workers for the development of protein-tethered lipid bilayers.[39,40] Ion-chelating nitrilotriacetic acid groups bearing a terminal amin group (N_{α},N_{α}-bis(carboxymethyl)-L-lysine hydrate [ANTA]) are coupled *in situ* to an *N*-hydroxy succinimide ester (NHS) functionalized surface. This surface was prepared by incubation of the gold electrode with di(*N*-succinimidyl) 3,3′-dithiodipropionate (DTSP). The resulting ANTA-decorated surface is activated by complexation of Cu^{2+} ions, rendering it capable of reversible immobilization of polyhistidine-tagged CMV-pp65 (Figure 1). In addition, the gate functionalization was completed by the addition of an oligo-(ethylene glycol)-terminated alkanethiol (OEG) passivating layer to cover the regions of the electrode not covered by ANTA, hence reducing the non-specific binding at the electrode. In fact, OEG layers are often exploited to prevent fouling processes at electrode surfaces while retaining hydrophilicity and increasing the characteristic Debye length of the interface.[41,42] This elegant strategy offers versatility to the functionalization process, as the polyhistidine tag is commonly used in recombinant protein production, allowing for the attachment of virtually any protein to the electrode surface. Moreover, because this tag is located at a specific position of the polypeptide chain (N or C terminus), it facilitates the formation of a more ordered biolayer on the electrode surface. This possibility is instead precluded by other standard electrode functionalization strategies, like the method exploiting the 1-Ethyl-3-(3-dimethylaminopropyl)carbodiimide/*N*-hydroxysuccinimide (EDC/NHS) coupling, which generally links proteins to a carboxylate self-assembled monolayer (SAM) on the electrode surface with a random orientation, hence possibly leading to differences in binding efficiencies depending on the protein orientation.

Please cite this article in press as: Manco Urbina et al., Dynamic studies of antibody-antigen interactions with an electrolyte-gated organic transistor, Cell Reports Physical Science (2024), https://doi.org/10.1016/j.xcrp.2024.101919

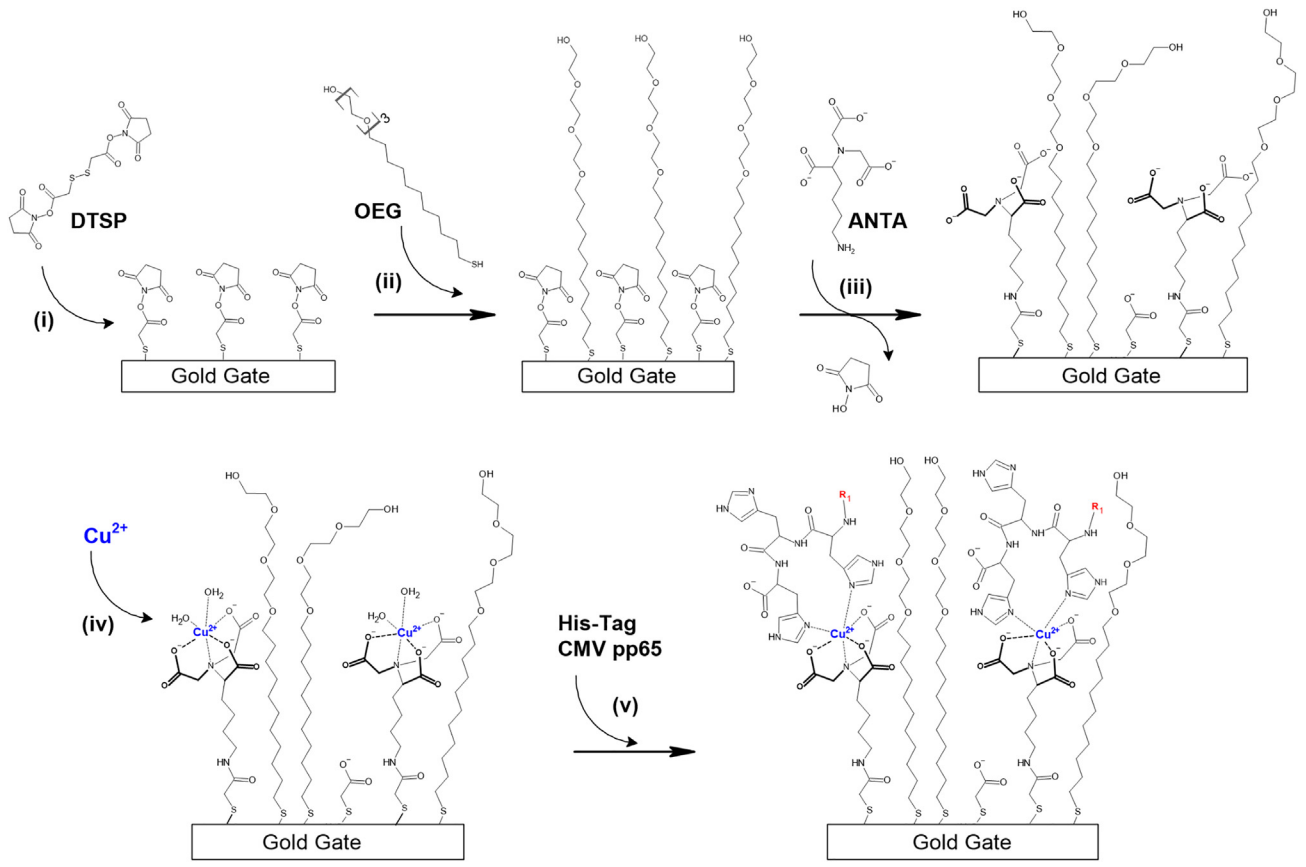

Figure 1. Au gate electrode functionalization methodology

The scheme describes the protocol I method, as reported in the text. An NHS-activated monolayer is prepared by self-assembly of DTSP on the Au surface (i). The gold surface was then incubated with OEG (ii) before the coupling with ANTA was performed (iii). Loading with Cu^{2+} was performed by immersing the electrode in a $CuSO_4$ solution (iv). The electrode surface was then ready for complexation with the His-tagged CMV-pp65 protein (v). The R_1 red labels represent the polypeptide chain of the CMV-pp65.

To optimize the density of binding sites of CMV-pp65 attached to the electrode, the effect of the OEG on the functionalization process was evaluated by testing three different experimental protocols: adding the OEG after DTSP (protocol I), adding the OEG after ANTA (protocol II), or without addition of OEG (protocol III) (see Note S1 for further details). To do this, each step of the functionalization process was optically monitored by fiber optic (FO) SPR in real time as shown in Figure 2A. The optical signal detection is based on the detuning of the resonant optical excitation of propagating surface plasmons at the metal-electrolyte interface due to local refractive index change. This change can be associated with mass adsorption at the metal surface.[43,44] Hence, the FO-SPR response allows one to estimate the amount of protein bound to the gold surface, corresponding to the number of available binding sites on the electrode surface (see experimental procedures).

The gold-coated FO was initially incubated with 50 mM phosphate buffer, 0.1% w/v BSA, 0.05% w/v Tween 20 (pH 7.4) until a stable optical signal was reached, which was then taken as the baseline signal. Afterward, the buffer solution was replaced with a Cu^{2+} solution to Cu load the ANTA, followed by a washing step with buffer and before incubation with a 600 nM polyhistidine-tagged CMV-pp65 protein solution. At this stage, buffer solution was then used to wash any protein not bound to the Cu^{2+}-ANTA binding sites. The resonance wavelength (λ_{SPR}) shift with respect

Please cite this article in press as: Manco Urbina et al., Dynamic studies of antibody-antigen interactions with an electrolyte-gated organic transistor, Cell Reports Physical Science (2024), https://doi.org/10.1016/j.xcrp.2024.101919

CellPress
OPEN ACCESS

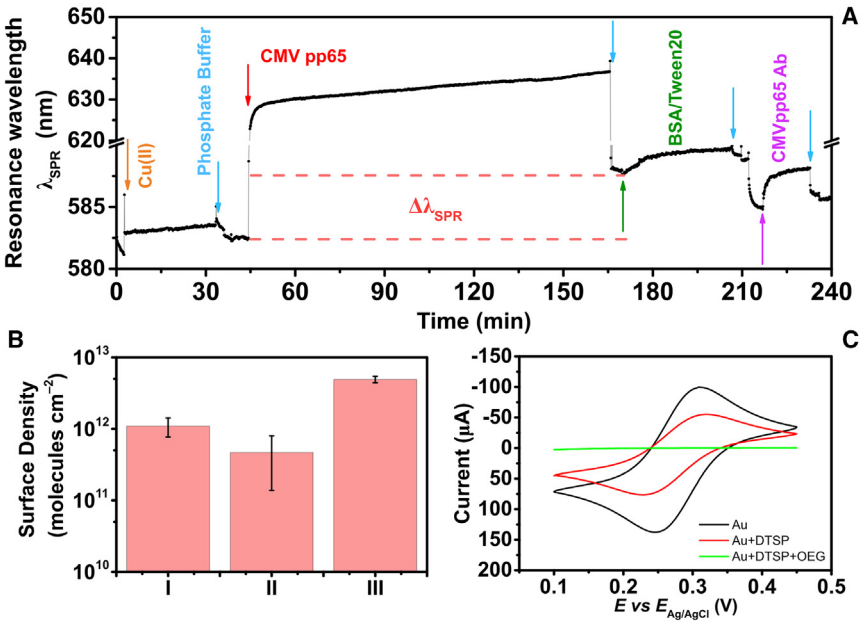

Figure 2. Characterization of the gate electrode functionalization

(A) SPR sensorgram of the gold surface functionalization process. Each reagent injection is represented by colored arrows.

(B) Comparison of CMV-pp65 adsorption efficiency of each tested protocol expressed in terms of average surface density (molecules cm^{-2}) with their associated standard deviations (based on three independent experiments).

(C) CV of the functionalized Au electrode using $K_3[Fe(CN)_6]$ as redox probe: bare Au, black trace; Au covered with DTSP-SAM, red trace; and Au covered with DTSP-SAM and OEG, green trace.

to the initial baseline is proportional to the amount of CMV-pp65 bound to the surface. The stability and the non-specific adsorption of this layer was then tested by incubation with a 0.1% w/v BSA, 0.05% w/v Tween 20 (pH 7.4) solution until equilibration of the optical signal. Washing with clean buffer restored the optical signal obtained at the previous step. Finally, the binding of the anti-CMV-Abs was demonstrated by incubating the FO with a 100 nM anti-CMV-Ab solution.

Figure 2B reports the amount of CMV-pp65 bound on the gold surface calculated from the SPR data (as reported in the experimental procedures): a higher coverage is obtained in the absence of the OEG layer (protocol III) compared with both protocols that included the formation of the OEG layer (protocols I and II), likely because of the steric hindrance due to the long OEG chains. On the other hand, the OEG addition before the incubation with the ANTA (protocol I) yielded a slightly higher CMV-pp65 surface density of 9.5 ($\pm$0.3) $\times$ 10^{11} molecules cm^{-2}, with respect to changing the addition order of these two reagents (protocol II).

Furthermore, the surface functionalization procedure was characterized through electrochemical methods using cyclic voltammetry in the presence of $[Fe(CN)_6]^{3-}$/$[Fe(CN)_6]^{4-}$ as a redox probe. Here, a gold wire was used as the working electrode to study the functionalization process. Upon functionalization of the electrode surface with the OEG/protein layers, the charge transfer resistance between the redox probe and the electrode increased, which reduced the faradaic current recorded with respect to the bare gold electrode. In the absence of OEG, the amount of CMV-pp65 protein is not sufficient to fully cover the electrode surface, which still presents faradaic current similar to the clean gold surface (Figure S1). During the

biosensing experiment, these exposed surfaces could lead to non-specific adsorption processes at the bare gold surface. Conversely, incubation with the OEG effectively passivates the electrode surface in the area that is not covered by the CMV-pp65, as demonstrated by the large faradaic current reduction (Figure 2C).

Based on these results, protocol I was selected to be implemented as the gate electrode functionalization strategy for anti-CMV-Ab detection with the EGOT device. This protocol yielded an average CMV-pp65 adsorbed density of 9.5 ($\pm$0.3) $\times$ 10^{11} molecules cm^{-2}, validating the use of this functionalization method to achieve high receptor densities of the electrode surface. In fact, this value is comparable to that of the surface coverage reported for other functionalization strategies that yield high receptor densities on the surface and characterized by SPR monitoring (4–8 $\times$ 10^{11} molecules cm^{-2}).[19,30,39,45]

Real-time biosensing

The EGOT conductive channel was fabricated by drop-casting of a PEDOT:PSS solution onto interdigitated gold source-drain electrodes (W/L = 50). A planar gold electrode on silicon substrate was used as the gate electrode and functionalized with CMV-pp65 as described above. The EGOT device was then integrated into a microfluidic system to perform the real-time sensing experiments.

The biosensing of the anti-CMV-Ab in buffered solutions (50 mM phosphate buffer [pH 7.4]) was performed by continuously monitoring the variations of I_{DS} vs. time, at constant V_{DS} = $-$0.2 V and V_{GS} = +0.5 V, for concentrations ranging from 1 to 500 nM anti-CMV-Ab in 50 mM phosphate buffer, 0.1% w/v BSA, 0.05% w/v Tween 20 (pH 7.4). Initially, the device was stabilized by flowing buffer solution through the microfluidic systems to obtain a constant current $I_{DS,0}$; then the device was exposed to increasing concentrations of anti-CMV-Abs by injecting the different standard solutions. Figure 3B (gray trace) shows a typical response of the EGOT sensor, where I_{DS} decreased rapidly upon analyte binding (red curve segments) and tended to attain a constant plateau. After the last standard sample, buffer solution (without analyte) was injected again into the microfluidic system, to induce the dissociation of the bound analyte. Indeed, an increase in the current was observed, indicating the reversibility of the binding process, although in the investigated time window we did not observe full recovery of the initial drain current value. In this figure, we note that the small kinks at the onset of the rise of each concentration step are likely due to small air bubbles entering the microfluidic system when the sample solutions are changed.

The decrease in I_{DS} magnitude is proportional to the anti-CMV-Ab concentration; hence, a calibration curve (Figure 3C) was constructed by measuring the sensor response in the steady-state regime of each concentration, that is to say, at the current plateau. The response was quantified in terms of signal (S), defined as the relative change in the current at a certain analyte concentration with respect to the initial value (in the absence of the analyte): $S = (I_{DS,0} - I_{DS})/I_{DS,0}$. The device demonstrates sensitivity to anti-CMV-Ab in solution by displaying a non-linear, monotonically increasing response as concentration rises from 1 to 500 nM. This non-linear calibration plot is a typical outcome in the field of EGOT biosensors[21,33,46] and, more in general, for methods based on ligand binding assays.[47,48] From these data, the quantitative relationship between S and anti-CMV-Ab concentration was obtained by fitting the signal with the Langmuir isotherm model, yielding an estimated binding constant K_L = 1.2 ($\pm$0.2) $\times$ 10^7 and an estimated maximum signal S_{max} = 0.82 (Figure 3C).[49,50] Furthermore, because the recorded signal is proportional to the

Please cite this article in press as: Manco Urbina et al., Dynamic studies of antibody-antigen interactions with an electrolyte-gated organic transistor, Cell Reports Physical Science (2024), https://doi.org/10.1016/j.xcrp.2024.101919

CellPress
OPEN ACCESS

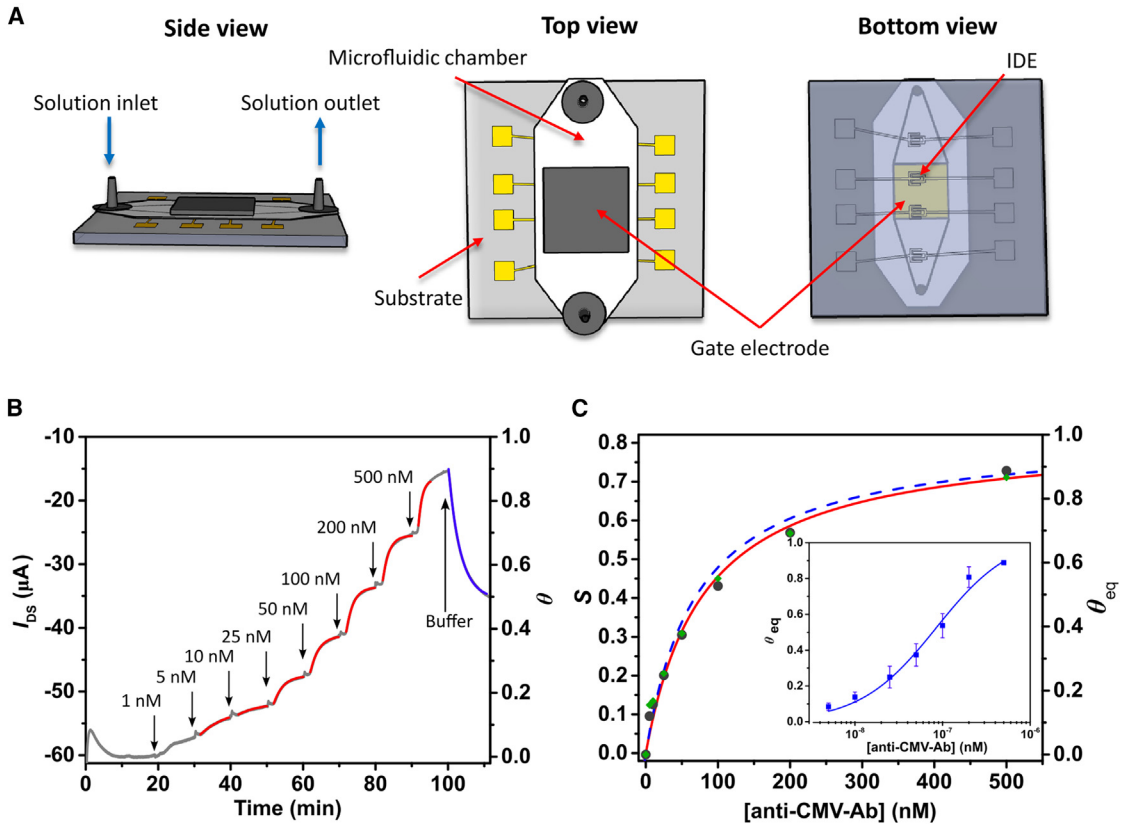

Figure 3. Real-time electrical sensing by functionalized gate electrode with CMV-pp65

(A) Scheme representing the microfluidics flow cell combined with the EGOT device used for biosensing.

(B) Sensor current variation to increasing concentrations of anti-CMV-Abs, plotted as I_{DS} vs. time (gray trace). The labeled arrows indicate the injection of the analyte standard solutions and of clean buffer. The red traces correspond to the fitting of the time-dependent θ changes (left axis) by kinetic analysis based on the two-compartment model. The blue trace represents the fitting of the debinding phase.

(C) Sensor calibration curve (black dots) expressed in terms of signal (S) and the corresponding surface coverage (θ) as a function of anti-CMV-Ab concentration. The red trace represents the fitting with the Langmuir isotherm model, giving an estimated K_L = 1.2 (±0.2) × 10^7 and S_{max} = 0.82. The blue dashed curve represents the Langmuir isotherm calculated with K_L = 1.5 ×10^7 obtained from the kinetic traces analysis. The green diamonds represent the steady-state θ_{eq} calculated from the two-compartment model from the fitting of the kinetic traces. Inset: average θ_{eq} (±SEM) vs. anti-CMV-Ab concentration (lin-log scale), together with the associated Langmuir isotherm fit (blue trace, K_L = 1.18 (±0.18) × 10^7); data points are presented as mean value ± SEM, based on a minimum of three to a maximum of five independent datasets. The 500 nM datapoint belongs to a single dataset.

amount of anti-CMV-Ab protein bound to the gate electrode surface, it is possible to convert the signal S into the surface fraction coverage (θ), defined as $\theta = S/S_{max}$, where S_{max} is the maximum signal estimated from the isotherm fitting. The coverage values are reported on the right axis of Figure 3B for θ vs. time, and Figure 3C for equilibrium surface coverage (θ_{eq}). In the inset of Figure 3C we show the average values of θ_{eq} over different datasets acquired. The continuous blue line is the best-fit Langmuir isotherm with K_L = 1.18 (±0.18) × 10^7.

Non-specific binding interactions at the channel or at gate-electrode surfaces are a common source of interference in the measured signal of a sensing experiment. Therefore, two different types of control experiments were performed to assess the specificity of the biosensor response to anti-CMV-Abs. In the first one, a solution containing 100 nM anti-IL-1β was used to test the device response to a different antibody; in the second one, 100 nM IL-6 was used to test the response to a molecule that has potentially increased levels in subjects with an active CMV infection. As described previously (see the introduction), the infection has been shown to induce

production of pro-inflammatory cytokines like IL-6 by leukocytes.[25] The non-specific response to 100 nM anti-IL-1β (Figure S2, light green background) has a significant signal, while the response to 100 nM IL-6 is, in practice, negligible (dark green background); however, both these signals are much lower than the specific response to anti-CMV-Abs (pink background) at the same concentration, indicating the satisfactory selectivity of the biosensor.

The theoretical LOD and limit of quantification (LOQ) were estimated following the IUPAC convention: these parameters are obtained from the standard deviation of the signal recorded when only phosphate buffer is fluxed into the system. This signal originates from the small fluctuations in the recorded current (I_{DS}) over time. The LOD and LOQ can be calculated using the relation $S_{(LOD/LOQ)} = S_0 + k\,\sigma$, where S_0 is the signal of the blank (which in this case is set to zero), σ is its associated standard deviation, and k is a factor that is set equal to 3 for the LOD and equal to 10 for the LOQ.[7,51] Here, σ was estimated as $\sigma = 0.002$, which corresponds to an LOD = 0.5 nM and an LOQ = 1.6 nM, on the basis of the Langmuir isotherm fit reported in Figure 3C. The samples at 1 nM concentration of anti-CMV-Abs generated a signal that was between the LOD and the LOQ and hence was not fully reliable for quantitative analysis; for this reason, they were excluded from the kinetics analysis presented in the next section. In addition, another possibility for the estimation of the theoretical LOD is to use the average signal obtained from the negative control experiments (Figure S2). Using this definition, and considering the average signal as S_0 with its associated standard deviation (n = 3 independent experiments), we obtained $LOD_{(anti\text{-}IL1\beta)}$ = 18 nM and $LOD_{(IL\text{-}6)}$ = 6 nM.

Kinetics analysis

The variation of the current over time obtained from the EGOT sensor, integrated into the microfluid system, allows us to extract information about the dynamics of the binding process. In this context, we adopted the TCM, which is one of the most widely exploited models for describing the binding kinetics of analytes in solution to surface-immobilized ligands under a constant flow rate of solution.[52,53] The TCM is commonly applied to the interpretation of SPR kinetics data and has been evoked also for electronic biosensors.[34,35] In the TCM, the binding kinetics results from a two-step process:

$$A_{(outer)} \overset{k_m}{\rightleftharpoons} A_{(inner)} + B_{(surf)} \underset{k_{off}}{\overset{k_{on}}{\rightleftharpoons}} AB_{(surf)}$$

The first step is the transport of the analyte (A, the anti-CMV-Ab in this case) from the bulk of the solution (termed here outer compartment) to the region close to the sensor surface (inner compartment). This step is followed by the reaction of the analyte with the binding site (B) anchored to the surface of the sensor ($B_{(surf)}$ is the binding site) (Figure S3).[52,53] Here, k_{on} is the second-order adsorption rate constant ($M^{-1}\,s^{-1}$), k_{off} (s^{-1}) is the first-order desorption rate constant, and k_m (s^{-1}) is the mass transport coefficient describing the diffusive motion of the analyte between the two compartments. This model is formulated in terms of a system of ordinary differential equations[38]:

$$V\frac{dC_s}{dt} = S[k_m L_D(C_0 - C_s) - k_{on}C_sP_0(1-\theta) + k_{off}P_0\theta], \qquad \text{(Equation 1)}$$

$$\frac{d\theta}{dt} = k_{on}C_s(1-\theta) - k_{off}\theta. \qquad \text{(Equation 2)}$$

The model approximates the outer compartment concentration C_0 as constant over time, while the concentration C_s of the analyte near the sensor surface changes over

Please cite this article in press as: Manco Urbina et al., Dynamic studies of antibody-antigen interactions with an electrolyte-gated organic transistor, Cell Reports Physical Science (2024), https://doi.org/10.1016/j.xcrp.2024.101919

CellPress
OPEN ACCESS

time because, on the one hand, the analyte is transported from the bulk of the solution with mass transport coefficient k_m, while on the other hand, it binds or dissociates from the binding site immobilized on the sensor surface with kinetic rate constant k_{on} or k_{off}, respectively. The electrode surface coverage θ is proportional to the amount of analyte bound to the receptor; P_0 is the maximum concentration of available binding sites (mol cm^{-2}); V (cm^3) is the volume of the inner compartment and S (cm^2) is the surface area of the sensor and L_D (cm) is the height of the inner compartment (related to the diffusion length) above the sensor surface.

The system formed by Equations 1 and 2 has no analytical solutions; hence, it can be solved only by numerical methods; however, under certain conditions it can be simplified, allowing one to determine analytical solutions. For example, in the regime where the analyte transport to the sensor surface is much faster than the binding reaction, the analyte concentration in the inner compartment can be considered constant ($C_s = C_0$) during the whole binding process: the model is then described only by Equation S4 and results in a simpler first-order binding kinetics (this model is often referred as the "rapid mixing model," Equation S5, also known as Langmuir binding kinetics).[34,38] On the other hand, mass transport effects will influence the binding kinetics when the association rate is comparable to or faster than the mass transport rate. In this situation, the term $k_m L_D (C_0 - C_s)$ cannot be neglected anymore, and it turns out that the model will depend on six parameters: k_{on}, k_{off}, k_m, L_D, P_0, and the ratio V/S (equivalent to the thickness of the inner compartment). However, previous studies demonstrated that the solutions to Equations 1 and 2 are insensitive to the value of V/S; in fact, works by Myszka et al. and Sigmundsson et al. showed that, once the binding or dissociation is initiated, C_s changes rapidly over a very short period of time (with respect to the binding kinetics time frame) and then very slowly thereafter.[38,54] Furthermore, while this rapid change in C_s is occurring, there is a negligible change in θ. This behavior implies that a quasi-steady-state approximation can be made where $dC_s/dt = 0$; hence, C_s is considered constant, but lower with respect to the bulk concentration.[38,55] With this condition, V/S drops out of Equation 1, explaining why the value of the ratio does not affect the final solution.

Under quasi-steady-state approximation, the model can be described by a single differential equation with the following form (see Note S2):

$$\frac{d\theta}{dt} = k_{on}\left(\frac{k'_m C_0 + k_{off}\theta}{k'_m + k_{on}(1-\theta)}\right)(1-\theta) - k_{off}\theta, \qquad \text{(Equation 3)}$$

where $k_m' = k_m L_D / P_0$ ($M^{-1}\ s^{-1}$), corresponding to the coefficient that can be extracted directly from the fitting procedure (as described below). From a physical point of view, this factor can still be considered as a mass transfer coefficient but, when expressed in $M^{-1}\ s^{-1}$, its numerical value also depends on the initial concentration of binding sites P_0.

In other terms, increasing the initial concentration of binding sites will cause a reduction of k_m', even if the flow rate of the system remains the same.

Equation 3 describes the formation of an analyte-ligand complex under partially limiting mass transport conditions. Sigmundsson et al. showed that the differential Equation 3 has an analytical solution, which takes the form[54]:

$$\theta = K_1\left[1 - \frac{1}{K_2} W\left(K_2 e^{(K_2 - K_3 k_{off}\ t)}\right)\right], \qquad \text{(Equation 4)}$$

where W represents the Lambert W function and

$$K_1 = \frac{k_{on}C_0}{k_{on}C_0+k_{off}}, \quad \text{(Equation 5)}$$

$$K_2 = \frac{k_{on}{}^2C_0}{(k_{on}C_0+k_{off})k'_m+k_{on}k_{off}}, \quad \text{(Equation 6)}$$

$$K_3 = \frac{(k_{on}C_0+k_{off})^2k'_m}{k_{off}\left[(k_{on}C_0+k_{off})k'_m+k_{on}k_{off}\right]}. \quad \text{(Equation 7)}$$

Hence, the exact solution, Equation 4, depends on four parameters, C_0, k_{on}, k_{off}, and k_m' (which contains P_0) The surface coverage θ(t = 0 s) equals 0, while for a long reaction time, the θ equilibrium value is equal to K_1:

$$\theta_{eq} = K_1 = \frac{k_{on}C_0}{k_{on}C_0+k_{off}} = \frac{K_LC_0}{K_LC_0+1}, \quad \text{(Equation 8)}$$

where $K_L = k_{on}/k_{off}$ is the thermodynamic equilibrium binding constant. Thus, Equation 8 describes the same equilibrium condition obtained from the Langmuir isotherm and from the rapid mixing model (Equations S4, and S5), as would be expected given that the constant flow of analyte solution tends toward a final constant concentration value equal to C_0.

To extract the kinetic and thermodynamic constants from the real-time binding experiments, the analytical solution, Equation 4, was then used to fit the kinetics data of θ vs. time, recorded at different initial concentrations C_0 of antibodies, using k_{on}, k_{off}, and k_m' as fitting parameters. The resulting best-fit curves are shown in Figure 3B as red traces overlaid with the experimental data (gray trace). One immediately notices the accuracy of the fitting throughout the set of data points. The values of the best-fit parameters extracted at each concentration are reported in Figure S4. Their average values are $k_{on} = 5.5\ (\pm 0.7) \times 10^4\ M^{-1}\ s^{-1}$, $k_{off} = 3.7\ (\pm 0.6) \times 10^{-3}\ s^{-1}$, and $k_m' = 3.8\ (\pm 0.3) \times 10^5\ M^{-1}\ s^{-1}$, where the experimental errors are reported as standard errors of the mean. The ratio $k_{on}/k_{off} = 1.5\ (\pm 0.3) \times 10^7\ M^{-1}$ closely matches the binding association constant $K_L = 1.2\ (\pm 0.2) \times 10^7$ obtained by the best fit of the steady-state data (plateaus) from Figure 3B as discussed above. The Langmuir isotherm obtained with $K_L = k_{on}/k_{off}$ is presented as a blue dashed line in Figure 3C. This result supports the adoption of the TCM to describe the binding process.

According to Equation 4, the coverage $\theta(t)$ exhibits a (quasi)exponential behavior (embedded in the Lambert function), whose inverse characteristic time is the observed association rate $k_{obs} = K_3k_{off}$. The calculation of the k_{obs} values is carried out at each concentration C_0 from each set of best-fit parameters. In the next paragraphs, we will show the puzzling outcome arising from two different data analyses that hints at the need of evaluating the level of approximations employed. At the same time, it underscores the importance of critically assessing these approximations and determining the more reliable approach between the two.

The first method for the data analysis is to use the average values of the kinetic parameters derived at each concentration C_0 (see previous paragraph) from the TCM model, which we will subsequently denote as the "TCM average." In this case, a linear relationship between k_{obs} and C_0 (Figure 4A, red markers and dashed line) emerges, similar to the one predicted by the rapid mixing model.[34,56] This trend would suggest that the overall association process is not significantly affected by mass transport effects, especially with the highest concentration samples, where a

Cell Reports
Physical Science
Article

CellPress
OPEN ACCESS

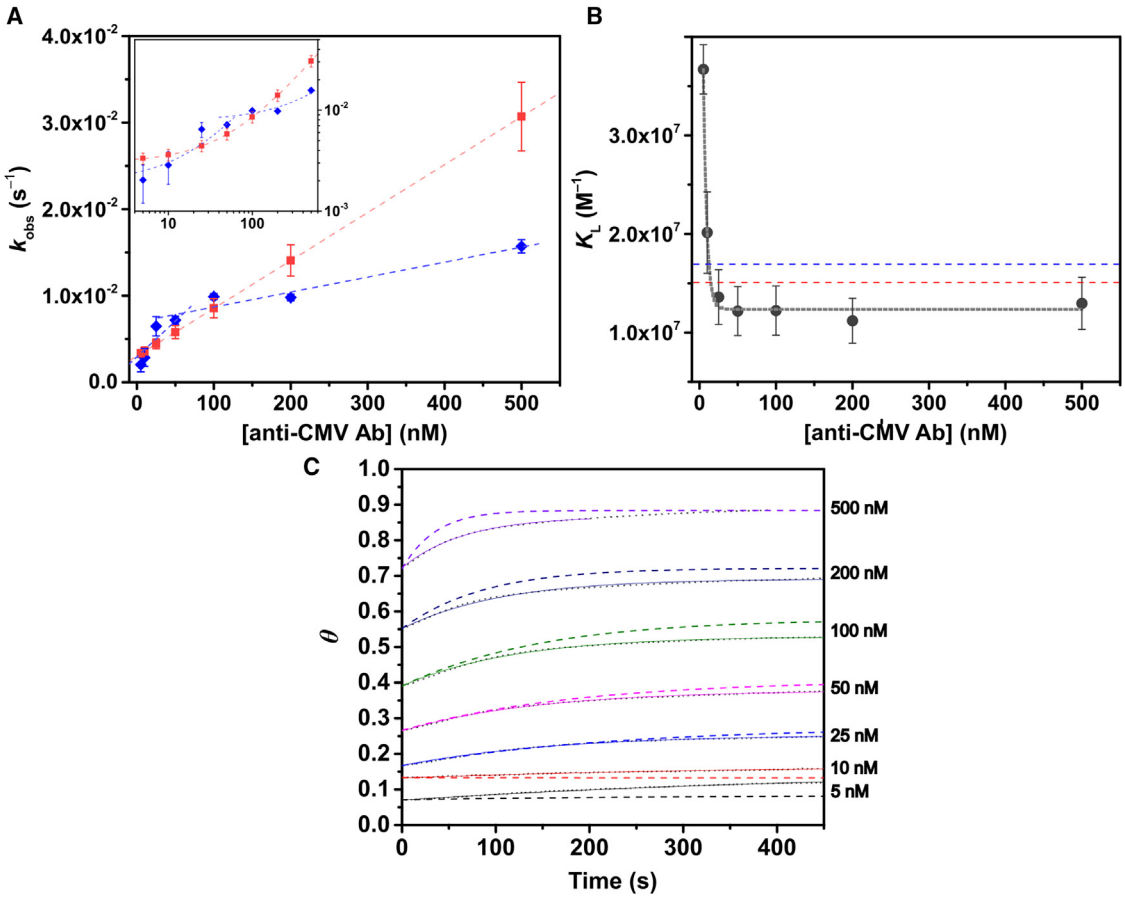

Figure 4. Analysis of binding kinetics

(A) Observed rate constants k_{obs}, as a function of analyte concentration, calculated using the average values of k_{on}, k_{off}, and k_m' obtained from the fittings with the two-compartment model ("TCM average," red squares and dashed line) and calculated using the k_{on}, k_{off}, and k_m' at the different analyte concentrations ("TCM local," blue diamonds), together with a qualitative (guide to the eye) representation of the two different linear regimes (blue dashed lines). Data points are reported as best-fit values ± SE, obtained from the fitting procedure. The inset shows the same plot on a log-log scale.

(B) Calculated binding constants (K_L) as k_{on}/k_{off} ratios as a function of analyte concentration. The blue line represents the average K_L value calculated with the local k_{on}/k_{off} ratios (TCM local), while the red one corresponds to the K_L obtained from the ratio k_{on}/k_{off} with their average values (TCM average). Data points are reported as calculated value ± SE, with SE calculated from the errors on k_{on} and k_{off}. The gray dotted line represents a guide to the eye for the trend of K_L vs. analyte concentration.

(C) Comparison between experimental kinetic traces (black dotted lines) with the kinetic traces calculated with the TCM (dashed lines) using the average k_{on}, k_{off}, and k_m' parameters extracted from the fitting procedure (TCM average) and the fitting using the local kinetic parameters (TCM local). The labels on the left axis indicate the sample analyte concentration.

high surface coverage (θ) is attained at the gate electrode. Indeed, the kinetics analysis shows that k_m' is substantially larger than k_{on}, with a ratio $k_m'/k_{on} \approx 6.5$. As a term of comparison, the systems that are strongly influenced by mass transfer effects generally exhibit $k_{on} \gg k_m'$.[38,56,57]

The second method calculates the k_{obs} values using the k_{on}, k_{off}, and k_m' best-fit values at each concentration, instead of using their average values (Figure 4A). Hereafter, this method will be denoted as "TCM local." Here, the outcome is a non-linear relationship between k_{obs} and C_0 (Figure 4A, blue markers and dashed line), different from the prediction by the rapid mixing model. At first glance, the trend of the blue markers seems to follow that of the red ones at low concentrations and to deviate from it at the higher concentrations. We notice that a crossover of the

Please cite this article in press as: Manco Urbina et al., Dynamic studies of antibody-antigen interactions with an electrolyte-gated organic transistor, Cell Reports Physical Science (2024), https://doi.org/10.1016/j.xcrp.2024.101919

trends of the blue and red data points occurs: while the trend of the red markers is definitely linear across the whole range of concentrations, the trend of the blue markers undergoes a transition between a steeper straight line (viz. higher k_{on} and smaller k_{off}) at the lowest concentrations and a less steep straight line at medium-high concentrations (viz. smaller k_{on} and higher k_{off}). We also notice that, for the series of the blue markers, the values of the mass transport coefficient k_m' are scattered around an average value of $k_m' = 3.8 \times 10^5\ M^{-1}\ s^{-1}$ (Figure S4).

While the available data do not conclusively identify the origin of this transition, we attempt a rationale in terms of the existence of a heterogeneous distribution of binding sites on the gate surface. At the simplest level, we envision the co-existence of two populations of binding sites: a minority with higher affinity (which implies higher K_L) and a majority with smaller affinity (and hence smaller K_L). Qualitatively, the blue dashed lines in Figure 4A illustrate this possibility: at the beginning of the experiment the binding sites with higher affinity are occupied first, resulting in a steeper slope (higher k_{on}); then, when these sites are saturated, the contribution of the binding sites with a lower affinity dominates the measured k_{obs}, resulting in a smaller slope and k_{on}. In terms of binding constant values, it is possible to make an educated guess based on the k_{on}/k_{off} ratios extracted at the different concentrations. From these values, at 5 nM $K_{L(high)} = 3.7 \times 10^7\ M^{-1}$, while at 500 nM $K_{L(low)} = 1.3 \times 10^7\ M^{-1}$, corresponding to a 3-fold reduction in binding constant (Figure 4B). The trend of the K_L values resembles a decaying exponential trend. The horizontal lines mark the mean K_L values (estimated either as the mean of the k_{on}/k_{off} ratio [blue] or the ratio of the mean k_{on} and the mean k_{off} [red line]).

The adoption of the local (in concentration) best-fit parameters is not explicitly contemplated by the TCM; however, it is convenient not to disregard it, as it explains the non-linear concentration dependence of the k_{obs}. The apparent existence of local rates hints at faster binding at low concentrations and slowing down of the kinetics at the highest analyte concentrations. Notably, the TCM does not foresee this transition, as it assumes a homogeneous distribution of binding sites with uniform affinity on the electrode surface.

In support of the existence of the non-linear concentration dependence of k_{obs}, we focus on the comparison of the experimental binding kinetics curves vs. time (Figure 4C, dotted lines) and their model-predicted counterparts calculated with the TCM average kinetic parameters (Figure 4C, dashed lines) and the TCM local kinetic parameters (Figure 4C, continuous line, and Figure 3B, red lines). Specifically, TCM average shows in general a good agreement at the shortest times and for medium concentrations (25–100 nM), while it overestimates the steady-state values. This behavior is also reflected in the positive shift of the blue dashed line in Figure 3C with respect to the equilibrium data point. On the other hand, TCM local maps the whole kinetics dataset. We infer that the analysis with the local values is more adherent to the actual kinetic process.

Finally, after the binding process with the highest anti-CMV-Ab concentration, the system was washed with buffer solution to allow the dissociation of the anti-CMV-Ab/CMV-pp65 complex. The kinetic trace for this dissociation phase can be fitted with an exponential function, assuming a first-order kinetics (Figure 3B, blue line). The result allows us to estimate the value of k_{off} independent of the previous fitting procedure (used in the association phase curves), yielding a value of $k_{off} = 4.9\ (\pm 0.5) \times 10^{-3}\ s^{-1}$, again comparable to the one obtained previously and further corroborating the degree of suitability of the TCM. Furthermore, this result suggests

Please cite this article in press as: Manco Urbina et al., Dynamic studies of antibody-antigen interactions with an electrolyte-gated organic transistor, Cell Reports Physical Science (2024), https://doi.org/10.1016/j.xcrp.2024.101919

CellPress
OPEN ACCESS

that for the 500 s after the injection of pure buffer, the dissociation rate is much slower than the transport rate, which makes the effect of the mass transport rate negligible and effectively reduces the initial phase of dissociation to a pseudo-first-order kinetics.

In summary, we report the fabrication of an EGOT biosensor in which we exploited the polyhistidine-tag technology to functionalize the gate electrode with a specific receptor for a target analyte. We applied this methodology to the detection of anti-CMV-Abs in solution. We demonstrated that, with this functionalization strategy, it is possible to obtain high receptor densities on the surface of the gate electrode, thus imparting high sensitivity in the nanomolar concentration range for anti-CMV-Abs. The polyhistidine-tag technology is a workhorse of recombinant protein purification technologies; hence, by making the functionalization strategy flexible and adaptable to a variety of analyte/receptor pairs, we may contribute to expanding the impact of this approach.

A central and important part of this work is the sensing in real time by continuous monitoring of the current vs. analyte binding to the gate electrode. Technologically, this required us to integrate the EGOT sensor into a microfluidic system. Scientifically, our analysis of the kinetics data vs. concentration of the anti-CMV-Abs showed that the observed kinetic rate of the time varying EGOT current has a non-linear dependence on the analyte concentration, which is not predicted by the simplest kinetic models of biorecognition at surfaces. We reconcile the experimental results with the TCM by introducing the co-existence of two populations of binding sites, each with different affinity toward the target and acting sequentially.

Our study highlights the remarkable sensitivity of EGOT for carrying out time-dependent experiments, as the device discriminates subtle features of the binding kinetics. To gain insights and give appropriate interpretation and values to the parameters, the adoption of binding models is essential. The quantitative evaluation of the biosensor's response time based on the functionalization strategy is central for further biosensor optimization and the screening of the surface chemistry strategies.

EXPERIMENTAL PROCEDURES

Resource availability

Lead contact

Further information and requests for resources should be directed to and will be fulfilled by the lead contact, Carlo Augusto Bortolotti (carloaugusto.bortolotti@unimore.it).

Materials availability

This study did not generate new unique materials.

Data and code availability

The authors declare that the data supporting the findings of this study are available within the article and the supplemental information. The raw data supporting the present study are available on the repository Zenodo: https://doi.org/10.5281/zenodo.10686960.

Gate functionalization

The gate functionalization strategy was adapted from the procedure reported by Giess et al.[39] Our method included an additional step in which the gate electrode was incubated with triethylene glycol mono-11-mercaptoundecyl ether, an OEG. The

Please cite this article in press as: Manco Urbina et al., Dynamic studies of antibody-antigen interactions with an electrolyte-gated organic transistor, Cell Reports Physical Science (2024), https://doi.org/10.1016/j.xcrp.2024.101919

effect of OEG addition on the binding of CMV-pp65 protein to the gate electrode was evaluated by testing three different protocols (reported in the supplemental information) and characterized with SPR. Eventually, the protocol used in the functionalization of the gate electrode for the biosensing experiments was as follows: (1) incubation of the gold electrode in 5 mM DTSP in dimethyl sulfoxide (DMSO) overnight, followed by (2) incubation in 100 μM OEG for 30 min; (3) incubation in 80 mM ANTA (pH 9.8), for 3 h; (4) incubation in 40 mM $CuSO_4$ in 50 mM acetate buffer (pH 5.5) for 30 min; (5) incubation in 0.05 mg mL^{-1} histidine-tagged CMV-pp65 in 50 mM phosphate buffer (pH 7.4) for 2 h, followed by a washing step with buffer and gentle drying with nitrogen; (6) final incubation in 0.1% BSA and 0.05% Tween 20 in 50 mM phosphate buffer (pH 7.4) for 30 min. Then the gate was inserted into the microfluidics system. All incubation steps were performed at room temperature.

Electrochemical characterization

The gate functionalization was monitored by cyclic voltammetry (CV) using a CH Instrument potentiostat model 760c. We performed the measurements in a three-electrode setup, using gold wire as the working electrode, platinum wire as the counter electrode, and Ag/AgCl as the reference electrode, working in 5 mM $K_3[Fe(CN)_6]$ and 1 M KCl solution, sweeping the potential between −0.2 and +0.6 V at a scan rate of 0.050 V s^{-1}.

Optical characterization

The functionalization process of the gold surface with the CMV-pp65 protein was optically monitored by SPR. As described by Hasler et al.,[17] FO tips were prepared to be used as SPR substrates by cleaving an optical fiber cladding exposing the glass fiber core at one end of the tip and subsequent sputter-coating with 50 nm of gold. White light was coupled to the fiber tip, where it resonantly excited surface plasmons within the optically active section at the end of the tip. Consequently, the light was back-reflected at the gold-coated cross section of the fiber tip and delivered to a spectrometer. The measured spectra with the tip contacting the liquid solution were normalized to those acquired with the tip in air. The gate functionalization was monitored starting from the FO functionalized with the DTSP-OEG-ANTA SAM in 50 mM phosphate buffer (pH 7.4).

The optical signal is presented as a shift of the resonance wavelength (λ_{SPR}), which corresponds to the minimum of the dip in the back-reflected spectrum. The shift of the resonance wavelength is related to local refractive index changes, associated with the molecular mass of the absorbed molecules at the gold surface/electrolyte interface. The measurement was performed in real time and in a label-free mode. From the shift of λ_{SPR}, it is possible to estimate the surface mass density Γ (ng cm^{-2}) according to the following equation[43,58]:

$$\Gamma = d_p (n_p - n_s) \left(\frac{\partial n}{\partial c}\right)^{-1}, \qquad \text{(Equation 9)}$$

where d_p is the biolayer thickness (derived from the λ_{SPR} using a simulated calibration curve as reported by Hasler et al.),[17] n_p and n_s are the refractive indexes of the biolayer and the electrolyte, respectively, and finally, $\partial n/\partial c$ is the coefficient relating the changes in the refractive index (n) with the adsorbed molecule concentration (c), which is typically set to 0.2 mm^3 mg^{-1} for biolayers.[59]

EGOT fabrication

For the EGOT-based biosensors, quartz test patterns were used, with 1 cm^2 of total area (as substrates purchased from Fondazione Bruno Kessler [FBK], Trento, Italy)

Please cite this article in press as: Manco Urbina et al., Dynamic studies of antibody-antigen interactions with an electrolyte-gated organic transistor, Cell Reports Physical Science (2024), https://doi.org/10.1016/j.xcrp.2024.101919

CellPress
OPEN ACCESS

with four interdigitated source and drain electrodes pairs, with a width/length ratio (*W/L*) equal to 50. Each quartz test pattern was initially rinsed with acetone, to remove the photoresist layer, and dried with a gentle nitrogen flow. This step was followed by a cleaning step in piranha solution (prepared by mixing 98% w/w H_2SO_4 and 30% v/v H_2O_2 at a 1:1 volume ratio) for 1 min at 150°C and abundant rinsing with water before the PEDOT:PSS deposition. The PEDOT:PSS used was prepared with 0.2% w/w curing agent and 5% w/w DMSO and then diluted 200 times in water. The final PEDOT:PSS solution was sonicated before use for at least 10 min and deposited on the substrate by drop-casting, followed by 30 min of thermal curing in the oven at 120°C. The transistor device was then completed using a gold wire as gate electrode and a 50 mM phosphate buffer (pH 7.4) as gating electrolyte. All electrical measurements were performed at room temperature inside a Faraday cage, using an Agilent B2912A source measure unit. Consecutive transfer curves were recorded until stabilization (as indicated by the overlap of at least the last five transfer curves), by sweeping the gate voltage (V_{GS}) from 0 to +0.6 V and keeping a constant drain-source voltage (V_{DS}) of −0.2 V. After stabilization, the device was incorporated into the microfluidics systems used for the biosensing measurements. In the EGOT device, the gate was a planar gold electrode on silicon substrate. The Au layer was deposited by evaporation, with a layer of chromium as the adhesion layer. The gate electrode was functionalized as reported above before the sensing experiments.

Microfluidics system setup and real-time biosensing

The EGOT device was integrated within a flexible bi-adhesive microfluidics as described previously.[60] The initial buffer was 50 mM phosphate (pH 7.4) containing 0.1% BSA and 0.05% Tween 20, which flowed through the microfluidics system dispensed by a peristaltic pump, working at 15 μL min^{-1}. The I_{DS} current was measured (V_{GS} = +0.5 V and V_{DS} = −0.2 V) over time until a stable baseline was obtained. Once the drain current had reached stability, the EGOT was exposed to increasing concentrations of anti-CMV-Abs, ranging from 1 to 500 nM, in 50 mM phosphate buffer, 0.1% BSA, 0.05% Tween 20 (pH 7.4). Control experiments were conducted by exposing the sensor to two different analytes to test the specific response of the biosensor. A solution of 100 nM anti-IL-1β antibody was used to test the response to a different antibody; a 100 nM solution of IL-6 was used to test the response to a possible interfering protein; both solutions were prepared in 50 mM phosphate buffer, 0.1% BSA, 0.05% Tween 20 (pH 7.4).

Analysis of the association-phase kinetics was performed by fitting each binding curve for a different concentration with Equation 4 using a MATLAB script. Minimization procedure was performed with the Levenberg-Marquardt algorithm, using the "lsqcurvefit" function available in MATLAB. For each step of the titration, t = 0 was defined as the onset of the current reduction after the sample injection, and the corresponding value of θ was taken as $\theta(t = 0)$. The fitting procedure allowed us to extract values for k_{on}, k_{off}, and k_m' at each different analyte concentration. The dissociation phase was fitted with a single exponential decay allowing us to extract the value of k_{off}.

Reagents

All the reagents and materials were used as provided from the manufacturer without further purification. Acetic acid, acetone, ANTA, BSA, copper (II) sulfate, (3-glycidyloxypropyl)trimethoxysilane (glymo), DMSO, DTSP, ethanol, hydrogen peroxide, 6-mercaptohexanol, triethylene glycol mono-11-mercaptoundecyl ether (the OEG),

phosphate salts, sodium acetate, sodium carbonate, sulfuric acid, and Tween 20 were purchased from Merk Sigma-Aldrich. PEDOT:PSS was purchased by Ossila. His-tagged CMV-pp65 (ab43041) and anti-CMV-Ab (1-L-11) were purchased from Abcam and Invitrogen, respectively. Anti-IL-1β Ab (JK1B-2) was purchased from BioLegend, while recombinant human IL-6 (cat.-no. 200-032) was from ReliaTech.

SUPPLEMENTAL INFORMATION

Supplemental information can be found online at https://doi.org/10.1016/j.xcrp.2024.101919.

ACKNOWLEDGMENTS

This project has received funding from the European Union's Horizon 2020 Research and Innovation Programme under the Marie Sklodowska-Curie grant agreement no. 813863. We further thank the Gesellschaft für Forschungsförderung (GFF) of Lower Austria for their financial support as part of the project "Aptamers and Odorant Binding Proteins – Innovative Receptors for Electronic Small Ligand Sensing" and the Czech Science Fund (GACR) for funding through the project APLOMA (22-30456J).

AUTHOR CONTRIBUTIONS

Conceptualization, C.A.B., F.B., M.P., and W.K.; methodology, P.A.M.U., R.H., M.S., M. Berto, P.G., J.D., C.A.B., F.B., and W.K.; investigation, P.A.M.U., R.H., and G.D.S.; formal analysis, A.P., P.A.M.U., M. Borsari, C.A.B., and F.B.; validation, P.A.M.U., A.P., and R.H.; writing – original draft, P.A.M.U., A.P., C.A.B., and F.B.; writing – review & editing, P.A.M.U., A.P., R.H., M.S., M. Berto, G.D.S, J.D., M.P., P.G., M. Borsari, W.K., C.A.B., and F.B.; funding acquisition, F.B., C.A.B., and W.K.; resources, C.A.B., W.K., and F.B.; supervision, C.A.B., W.K., P.G., and F.B.

DECLARATION OF INTERESTS

The authors declare no competing interests.

Received: January 3, 2024
Revised: February 23, 2024
Accepted: March 17, 2024
Published: April 16, 2024

REFERENCES

1. Rogers, K.R. (2000). Principles of Affinity-Based Biosensors. Mol. Biotechnol. *14*, 109–129. https://doi.org/10.1385/MB:14:2:109.

2. Scarano, S., Mascini, M., Turner, A.P.F., and Minunni, M. (2010). Surface plasmon resonance imaging for affinity-based biosensors. Biosens. Bioelectron. *25*, 957–966. https://doi.org/10.1016/j.bios.2009.08.039.

3. Yoon, J., Cho, H.Y., Shin, M., Choi, H.K., Lee, T., and Choi, J.W. (2020). Flexible electrochemical biosensors for healthcare monitoring. J. Mater. Chem. B *8*, 7303–7318. https://doi.org/10.1039/D0TB01325K.

4. Torricelli, F., Adrahtas, D.Z., Bao, Z., Berggren, M., Biscarini, F., Bonfiglio, A., Bortolotti, C.A., Frisbie, C.D., Macchia, E., Malliaras, G.G., et al. (2021). Electrolyte-gated transistors for enhanced performance bioelectronics. Nature Reviews Methods Primers *1*, 66. https://doi.org/10.1038/s43586-021-00065-8.

5. Pappa, A.-M., Parlak, O., Scheiblin, G., Mailley, P., Salleo, A., and Owens, R.M. (2018). Organic Electronics for Point-of-Care Metabolite Monitoring. Trends Biotechnol. *36*, 45–59. https://doi.org/10.1016/j.tibtech.2017.10.022.

6. Rivnay, J., Owens, R.M., and Malliaras, G.G. (2014). The Rise of Organic Bioelectronics. Chem. Mater. *26*, 679–685. https://doi.org/10.1021/cm4022003.

7. Torsi, L., Magliulo, M., Manoli, K., and Palazzo, G. (2013). Organic field-effect transistor sensors: a tutorial review. Chem. Soc. Rev. *42*, 8612–8628. https://doi.org/10.1039/c3cs60127g.

8. Wang, D., Noël, V., and Piro, B. (2016). Electrolytic Gated Organic Field-Effect Transistors for Application in Biosensors—A Review. Electronics (Basel) *5*, 9. https://doi.org/10.3390/electronics5010009.

9. He, Q., Wu, S., Yin, Z., and Zhang, H. (2012). Graphene-based electronic sensors. Chem. Sci. *3*, 1764. https://doi.org/10.1039/c2sc20205k.

10. Shi, S., Chen, F., Ehlerding, E.B., and Cai, W. (2014). Surface Engineering of Graphene-Based Nanomaterials for Biomedical Applications. Bioconjug Chem *25*, 1609–1619. https://doi.org/10.1021/bc500332c.

11. Lee, C.S., Gwyther, R.E.A., Freeley, M., Jones, D., and Palma, M. (2022). Fabrication and Functionalisation of Nanocarbon-Based Field-Effect Transistor Biosensors. Chembiochem. *23*, e202200282. https://doi.org/10.1002/cbic.202200282.

12. Molazemhosseini, A., Viola, F.A., Berger, F.J., Zorn, N.F., Zaumseil, J., and Caironi, M. (2021). A Rapidly Stabilizing Water-Gated Field-Effect Transistor Based on Printed Single-Walled Carbon Nanotubes for Biosensing

Please cite this article in press as: Manco Urbina et al., Dynamic studies of antibody-antigen interactions with an electrolyte-gated organic transistor, Cell Reports Physical Science (2024), https://doi.org/10.1016/j.xcrp.2024.101919

Applications. ACS Appl. Electron. Mater. *3*, 3106–3113. https://doi.org/10.1021/acsaelm.1c00332.

13. Paradisi, A., Berto, M., Di Giosia, M., Mazzali, S., Borsari, M., Marforio, T.D., Zerbetto, F., Calvaresi, M., Orieshyna, A., Amdursky, N., et al. (2023). Robust Biosensor Based on Carbon Nanotubes/Protein Hybrid Electrolyte Gated Transistors. Eur. J. Chem. *29*, e202301704. https://doi.org/10.1002/chem.202301704.

14. Xu, X., Bowen, B.J., Gwyther, R.E.A., Freeley, M., Grigorenko, B., Nemukhin, A.V., Eklöf-Österberg, J., Moth-Poulsen, K., Jones, D.D., and Palma, M. (2021). Tuning Electrostatic Gating of Semiconducting Carbon Nanotubes by Controlling Protein Orientation in Biosensing Devices. Angew. Chem. Int. Ed. *60*, 20184–20189. https://doi.org/10.1002/anie.202104044.

15. Dankerl, M., Hauf, M.V., Lippert, A., Hess, L.H., Birner, S., Sharp, I.D., Mahmood, A., Mallet, P., Veuillen, J.-Y., Stutzmann, M., and Garrido, J.A. (2010). Graphene Solution-Gated Field-Effect Transistor Array for Sensing Applications. AdvAdv. Funct. Mater. *20*, 3117–3124. https://doi.org/10.1002/adfm.201000724.

16. Sensi, M., de Oliveira, R.F., Berto, M., Palmieri, M., Ruini, E., Livio, P.A., Conti, A., Pinti, M., Salvarani, C., Cossarizza, A., et al. (2023). Reduced Graphene Oxide Electrolyte-Gated Transistor Immunosensor with Highly Selective Multiparametric Detection of Anti-Drug Antibodies. Adv Mater *35*. https://doi.org/10.1002/adma.202211352.

17. Hasler, R., Reiner-Rozman, C., Fossati, S., Aspermair, P., Dostalek, J., Lee, S., Ibáñez, M., Bintinger, J., and Knoll, W. (2022). Field-Effect Transistor with a Plasmonic Fiber Optic Gate Electrode as a Multivariable Biosensor Device. ACS Sens. *7*, 504–512. https://doi.org/10.1021/acssensors.1c02313.

18. Chen, S., Sun, Y., Fan, X., Xu, Y., Chen, S., Zhang, X., Man, B., Yang, C., and Du, J. (2023). Review on two-dimensional material-based field-effect transistor biosensors: accomplishments, mechanisms, and perspectives. J Nanobiotechnology *21*, 144. https://doi.org/10.1186/s12951-023-01898-z.

19. Sarcina, L., Torsi, L., Picca, R.A., Manoli, K., and Macchia, E. (2020). Assessment of Gold Bio-Functionalization for Wide-Interface Biosensing Platforms. Sensors *20*, 3678. https://doi.org/10.3390/s20133678.

20. White, S.P., Dorfman, K.D., and Frisbie, C.D. (2016). Operating and Sensing Mechanism of Electrolyte-Gated Transistors with Floating Gates: Building a Platform for Amplified Biodetection. J. Phys. Chem. C *120*, 108–117. https://doi.org/10.1021/acs.jpcc.5b10694.

21. Berto, M., Casalini, S., Di Lauro, M., Marasso, S.L., Cocuzza, M., Perrone, D., Pinti, M., Cossarizza, A., Pirri, C.F., Simon, D.T., et al. (2016). Biorecognition in Organic Field Effect Transistors Biosensors: The Role of the Density of States of the Organic Semiconductor. Anal. Chem. *88*, 12330–12338. https://doi.org/10.1021/acs.analchem.6b03522.

22. Rivnay, J., Inal, S., Salleo, A., Owens, R.M., Berggren, M., and Malliaras, G.G. (2018). Organic electrochemical transistors. NatNat. Rev. Mater. *3*, 17086. https://doi.org/10.1038/natrevmats.2017.86.

23. Palazzo, G., De Tullio, D., Magliulo, M., Mallardi, A., Intranuovo, F., Mulla, M.Y., Favia, P., Vikholm-Lundin, I., and Torsi, L. (2015). Detection Beyond Debye's Length with an Electrolyte-Gated Organic Field-Effect Transistor. Adv Mater *27*, 911–916. https://doi.org/10.1002/adma.201403541.

24. Pawelec, G., Larbi, A., and Derhovanessian, E. (2010). Senescence of the Human Immune System. J. Comp. Pathol. *142*, S39–S44. https://doi.org/10.1016/j.jcpa.2009.09.005.

25. Hummel, M., and Abecassis, M.M. (2002). A model for reactivation of CMV from latency. J. Clin. Virol. *25*, 123–136. https://doi.org/10.1016/S1386-6532(02)00088-4.

26. Wikby, A., Nilsson, B.-O., Forsey, R., Thompson, J., Strindhall, J., Löfgren, S., Ernerudh, J., Pawelec, G., Ferguson, F., and Johansson, B. (2006). The immune risk phenotype is associated with IL-6 in the terminal decline stage: Findings from the Swedish NONA immune longitudinal study of very late life functioning. Mech. Ageing Dev. *127*, 695–704. https://doi.org/10.1016/j.mad.2006.04.003.

27. Freeman, R.B. (2009). The 'Indirect' Effects of Cytomegalovirus Infection. Am. J. Transplant *9*, 2453–2458. https://doi.org/10.1111/j.1600-6143.2009.02824.x.

28. Berto, M., Casalini, S., Di Lauro, M., Marasso, S.L., Cocuzza, M., Perrone, D., Pinti, M., Cossarizza, A., Pirri, C.F., Simon, D.T., et al. (2016). Biorecognition in organic field effect transistors biosensors: The role of the density of states of the organic semiconductor. Anal. Chem. *88*, 12330–12338. https://doi.org/10.1021/ACS.ANALCHEM.6B03522/SUPPL_FILE/AC6B03522_SI_001.PDF.

29. Piro, B., Wang, D., Benaoudia, D., Tibaldi, A., Anquetin, G., Noël, V., Reisberg, S., Mattana, G., and Jackson, B. (2017). Versatile transduction scheme based on electrolyte-gated organic field-effect transistor used as immunoassay readout system. Biosens. Bioelectron. *92*, 215–220. https://doi.org/10.1016/j.bios.2017.02.020.

30. Macchia, E., Manoli, K., Holzer, B., Di Franco, C., Ghittorelli, M., Torricelli, F., Alberga, D., Mangiatordi, G.F., Palazzo, G., Scamarcio, G., and Torsi, L. (2018). Single-molecule detection with a millimetre-sized transistor. Nat. Commun. *9*, 3223. https://doi.org/10.1038/s41467-018-05235-z.

31. Macchia, E., Manoli, K., Di Franco, C., Picca, R.A., Österbacka, R., Palazzo, G., Torricelli, F., Scamarcio, G., and Torsi, L. (2020). Organic Field-Effect Transistor Platform for Label-Free, Single-Molecule Detection of Genomic Biomarkers. ACS Sens. *5*, 1822–1830. https://doi.org/10.1021/ACSSENSORS.0C00694/ASSET/IMAGES/MEDIUM/SE0C00694_M002.GIF.

32. Genco, E., Modena, F., Sarcina, L., Björkström, K., Brunetti, C., Caironi, M., Caputo, M., Demartis, V.M., Di Franco, C., Frusconi, G., et al. (2023). A Single-Molecule Bioelectronic Portable Array for Early Diagnosis of Pancreatic Cancer Precursors. Adv Mater *35*. https://doi.org/10.1002/adma.202304102.

33. Manco Urbina, P.A., Berto, M., Greco, P., Sensi, M., Borghi, S., Borsari, M., Bortolotti, C.A., and Biscarini, F. (2021). Physical insights from the Frumkin isotherm applied to electrolyte gated organic transistors as protein biosensors. J Mat Chem C *9*, 10965–10974. https://doi.org/10.1039/D1TC02546E.

34. Duan, X., Li, Y., Rajan, N.K., Routenberg, D.A., Modis, Y., and Reed, M.A. (2012). Quantification of the affinities and kinetics of protein interactions using silicon nanowire biosensors. Nat. Nanotechnol. *7*, 401–407. https://doi.org/10.1038/nnano.2012.82.

35. Hammock, M.L., Knopfmacher, O., Naab, B.D., Tok, J.B.-H., and Bao, Z. (2013). Investigation of Protein Detection Parameters Using Nanofunctionalized Organic Field-Effect Transistors. ACS Nano *7*, 3970–3980. https://doi.org/10.1021/nn305903q.

36. Larisika, M., Kotlowski, C., Steininger, C., Mastrogiacomo, R., Pelosi, P., Schütz, S., Peteu, S.F., Kleber, C., Reiner-Rozman, C., Nowak, C., and Knoll, W. (2015). Electronic Olfactory Sensor Based on A. mellifera Odorant-Binding Protein 14 on a Reduced Graphene Oxide Field-Effect Transistor. Angew. Chem. *127*, 13443–13446. https://doi.org/10.1002/ANGE.201505712.

37. Selvaraj, M., Greco, P., Sensi, M., Saygin, G.D., Bellassai, N., D'Agata, R., Spoto, G., and Biscarini, F. (2021). Label free detection of miRNA-21 with electrolyte gated organic field effect transistors (EGOFETs). Biosens. Bioelectron. *182*, 113144. https://doi.org/10.1016/j.bios.2021.113144.

38. Myszka, D.G., He, X., Dembo, M., Morton, T.A., and Goldstein, B. (1998). Extending the Range of Rate Constants Available from BIACORE: Interpreting Mass Transport-Influenced Binding Data. Biophys. J. *75*, 583–594. https://doi.org/10.1016/S0006-3495(98)77549-6.

39. Giess, F., Friedrich, M.G., Heberle, J., Naumann, R.L., and Knoll, W. (2004). The Protein-Tethered Lipid Bilayer: A Novel Mimic of the Biological Membrane. Biophys. J. *87*, 3213–3220. https://doi.org/10.1529/biophysj.104.046169.

40. Ataka, K., Giess, F., Knoll, W., Naumann, R., Haber-Pohlmeier, S., Richter, B., and Heberle, J. (2004). Oriented Attachment and Membrane Reconstitution of His-Tagged Cytochrome *c* Oxidase to a Gold Electrode: In Situ Monitoring by Surface-Enhanced Infrared Absorption Spectroscopy. JJ. Am. Chem. Soc. *126*, 16199–16206. https://doi.org/10.1021/ja045951h.

41. Haustein, N., Gutiérrez-Sanz, Ó., and Tarasov, A. (2019). Analytical Model To Describe the Effect of Polyethylene Glycol on Ionic Screening of Analyte Charges in Transistor-Based Immunosensing. ACS Sens. *4*, 874–882. https://doi.org/10.1021/acssensors.8b01515.

42. Zheng, Z., Zhang, H., Zhai, T., and Xia, F. (2021). Overcome Debye Length Limitations for Biomolecule Sensing Based on Field Effective Transistors. Chin. J. Chem. *39*, 999–1008. https://doi.org/10.1002/cjoc.202000584.

43. Homola, J., Yee, S.S., and Gauglitz, G. (1999). Surface plasmon resonance sensors: review. Sens Actuators B Chem *54*, 3–15. https://doi.org/10.1016/S0925-4005(98)00321-9.

Please cite this article in press as: Manco Urbina et al., Dynamic studies of antibody-antigen interactions with an electrolyte-gated organic transistor, Cell Reports Physical Science (2024), https://doi.org/10.1016/j.xcrp.2024.101919

44. Baio, J.E., Graham, D.J., and Castner, D.G. (2020). Surface analysis tools for characterizing biological materials. Chem. Soc. Rev. *49*, 3278–3296. https://doi.org/10.1039/D0CS00181C.

45. Holzer, B., Manoli, K., Ditaranto, N., Macchia, E., Tiwari, A., Di Franco, C., Scamarcio, G., Palazzo, G., and Torsi, L. (2017). Characterization of Covalently Bound Anti-Human Immunoglobulins on Self-Assembled Monolayer Modified Gold Electrodes. Adv Biosyst *1*, 1700055. https://doi.org/10.1002/adbi.201700055.

46. Nakatsuka, N., Yang, K.A., Abendroth, J.M., Cheung, K.M., Xu, X., Yang, H., Zhao, C., Zhu, B., Rim, Y.S., Yang, Y., et al. (2018). Aptamer-field-effect transistors overcome Debye length limitations for small-molecule sensing. Science (1979 *362*, 319–324. https://doi.org/10.1126/science.aao675.

47. Wilson, B.D., and Soh, H.T. (2020). Re-Evaluating the Conventional Wisdom about Binding Assays. Trends Biochem. Sci. *45*, 639–649. https://doi.org/10.1016/J.TIBS.2020.04.005.

48. Findlay, J.W.A., and Dillard, R.F. (2007). Appropriate calibration curve fitting in ligand binding assays. AAPS J. *9*, E260–E267. https://doi.org/10.1208/aapsj0902029.

49. Langmuir, I. (1918). The adsorption of gases on plane surfaces of glass, mica and platinum. JJ. Am. Chem. Soc. *40*, 1361–1403. https://doi.org/10.1021/JA02242A004/ASSET/JA02242A004.FP.PNG_V03.

50. Swenson, H., and Stadie, N.P. (2019). Langmuir's Theory of Adsorption: A Centennial Review. Langmuir. *35*, 5409–5426. https://doi.org/10.1021/acs.langmuir.9b00154.

51. A.D. McNaught, and A. Wilkinson, eds. (1997). IUPAC. Compendium of Chemical Terminology, 2nd ed. (Blackwell Scientific Publications).

52. Myszka, D.G. (1997). Kinetic analysis of macromolecular interactions using surface plasmon resonance biosensors. Curr. Opin. Biotechnol. *8*, 50–57. https://doi.org/10.1016/S0958-1669(97)80157-7.

53. Myszka, D.G., Arulanantham, P.R., Sana, T., Wu, Z., Morton, T.A., and Ciardelli, T.L. (1996). Kinetic analysis of ligand binding to interleukin-2 receptor complexes created on an optical biosensor surface. Protein Sci. *5*, 2468–2478. https://doi.org/10.1002/pro.5560051209.

54. Sigmundsson, K., Másson, G., Rice, R., Beauchemin, N., and Öbrink, B. (2002). Determination of Active Concentrations and Association and Dissociation Rate Constants of Interacting Biomolecules: An Analytical Solution to the Theory for Kinetic and Mass Transport Limitations in Biosensor Technology and Its Experimental Verification. Biochem *41*, 8263–8276. https://doi.org/10.1021/bi020099h.

55. Segel, L.A., and Slemrod, M. (1989). The Quasi-Steady-State Assumption: A Case Study in Perturbation. SIAM Rev. *31*, 446–477.

56. Schuck, P. (1997). Use of Surface Plasmon Resonance to Probe the Equilibrium and Dynamic Aspects of Interactions Between Biological Macromolecules. Annu. Rev. Biophys. Biomol. Struct. *26*, 541–566. https://doi.org/10.1146/annurev.biophys.26.1.541.

57. Schuck, P., and Minton, A.P. (1996). Analysis of Mass Transport-Limited Binding Kinetics in Evanescent Wave Biosensors. Anal. Biochem. *240*, 262–272. https://doi.org/10.1006/abio.1996.0356.

58. Homola, J. (2008). Surface Plasmon Resonance Sensors for Detection of Chemical and Biological Species. Chem Rev *108*, 462–493. https://doi.org/10.1021/cr068107d.

59. Perlmann, G.E., and Longsworth, L.G. (1948). The Specific Refractive Increment of Some Purified Proteins. JJ. Am. Chem. Soc. *70*, 2719–2724. https://doi.org/10.1021/ja01188a027.

60. Parkula, V., Berto, M., Diacci, C., Patrahau, B., Di Lauro, M., Kovtun, A., Liscio, A., Sensi, M., Samorì, P., Greco, P., et al. (2020). Harnessing Selectivity and Sensitivity in Electronic Biosensing: A Novel Lab-on-Chip Multigate Organic Transistor. Anal. Chem. *92*, 9330–9337. https://doi.org/10.1021/acs.analchem.0c01655.